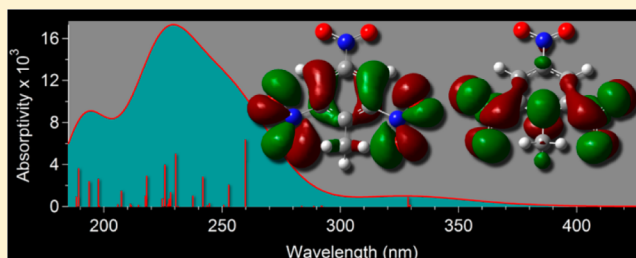# Experimental and TD-DFT Study of Optical Absorption of Six Explosive Molecules: RDX, HMX, PETN, TNT, TATP, and HMTD

Jason K. Cooper,[†] Christian D. Grant,*,[‡] and Jin Z. Zhang*,[†]

[†]Department of Chemistry and Biochemistry, University of California, Santa Cruz, California 95064, United States

[‡]Physical and Life Sciences, Chemical Sciences Division, Lawrence Livermore National Laboratory, 7000 East Avenue, Livermore, California 94550, United States

S Supporting Information

ABSTRACT: Time dependent density function theory (TD-DFT) has been utilized to calculate the excitation energies and oscillator strengths of six common explosives: RDX (1,3,5-trinitroperhydro-1,3,5-triazine), β-HMX (octahydro-1,3,5,7-tetranitro-1,3,5,7-tetrazocine), TATP (triacetone triperoxide), HMTD (hexamethylene triperoxide diamine), TNT (2,4,6-trinitrotoluene), and PETN (pentaerythritol tetranitrate). The results were compared to experimental UV−vis absorption spectra collected in acetonitrile. Four computational methods were tested including: B3LYP, CAM-B3LYP, ωB97XD, and PBE0. PBE0 outperforms the other methods tested. Basis set effects on the electronic energies and oscillator strengths were evaluated with 6-31G(d), 6-31+G(d), 6-31+G(d,p), and 6-311+G(d,p). The minimal basis set required was 6-31+G(d); however, additional calculations were performed with 6-311+G(d,p). For each molecule studied, the natural transition orbitals (NTOs) were reported for the most prominent singlet excitations. The TD-DFT results have been combined with the IP_v calculated by CBS-QB3 to construct energy level diagrams for the six compounds. The results suggest optimization approaches for fluorescence based detection methods for these explosives by guiding materials selections for optimal band alignment between fluorescent probe and explosive analyte. Also, the role of the TNT Meisenheimer complex formation and the resulting electronic structure thereof on of the quenching mechanism of II−VI semiconductors is discussed.

1. INTRODUCTION

The detection and quantification of explosive molecules continues to be an active area of research with various security and military applications. Many laboratory-based approaches have been developed to detect these types of molecules including pulse laser ionization time-of-flight mass spectroscopy,[1−3] laser induced photofragmentation,[4] ion mobility spectrometry,[5,6] HPLC-diode array detection,[7,8] LC/MS-atmospheric pressure chemical ionization,[9] and Raman.[10,11] In addition, detection methods based on colorimetry[12,13] and fluorescence[14,15] have been developed. Although laboratory-based methods offer high sensitivity and specificity, colorimetric and fluorescence methods are both lower in cost and easier for field deployment. Colorimetric methods utilize a reagent that produces a color change when reacted with the target analyte. Fluorescence-based approaches typically monitor luminescence intensity changes of a probe exposed to an explosive analyte.

Although there have been several reports utilizing different fluorescent probes, quantum dots (QDs) made from CdSe,[16] CdTe,[17,18] CdTe/CdS,[19] CdSe/ZnS,[20] and ZnS:Mn[21] have received increasing attention due to their size tunable emission spectrum, high fluorescence quantum yield, and stability against photobleaching. A recent report using QD as the fluorescence probe reported the detection of TNT on manila envelope substrates achieving detection limits of 5 ng mm^{-2}.[17] The

application of QD based detection methods has been limited to TNT, wherein the binding mechanism to the QD probe has been through the formation of Meisenheimer complexes in which QD bound primary amine capping ligands bond with the electron deficient TNT molecule at the same ring site as the methyl group.[22] Conjugated fluorescent polymers have proven to be very effective in the detection of TNT in the gas phase[23] and surfaces,[24] and to the detection of a wide range of other explosives,[25−28] whereas thin layer chromatographic plates containing a fluorescent polymer are effective in increasing selectivity while maintaining low detection limits.[29] For both probe types described above, the mechanism of detection is through luminescence quenching. That is, the amount of quenching is directly related to the concentration of the target analyte. One possible fluorescence quenching mechanism involves the photoexcitation to an excited state of a probe molecule or QD with subsequent excitation transfer to a nearby analyte that has an electronic acceptor state energetically below the excited state of the probe. The relaxation that follows is

nonradiative and is typically back-transfer to the ground state of the probe. Therefore, detailed knowledge of the energy levels of the target analyte and its vertical and adiabatic electron affinities (EA_V and EA_A, respectively) is critical to understanding this mechanism further.

For many of the above-described methods, the absorption of light by the target analyte plays a critical role in the detection methodology. For most energetic molecules, the absorption of light is in the UV to deep UV region. Consequently, pulsed laser induced photoionization can utilize multiphoton ionization from a low energy excitation source.[2,30,31] Of course, nonlinear absorption is very sensitive to pump fluence,[32] making knowledge of the ionization energy critical to the optimization of target ionization while minimizing background interference.

As a companion to our previous study in which we reported the IP and EA for the same six explosives,[33] we have characterized the singlet transitions by TD-DFT and report the natural transition orbitals (NTOs)[34] associated with the UV to deep UV excitations for six explosives: RDX (hexogen), β-HMX (octogen), TATP (triacetone triperoxide), HMTD (hexamethylene triperoxide diamine), TNT (2,4,6-trinitrotoluene), and PETN (pentaerythritol tetranitrate). Their molecular structures are shown in Figure 1. The excited state
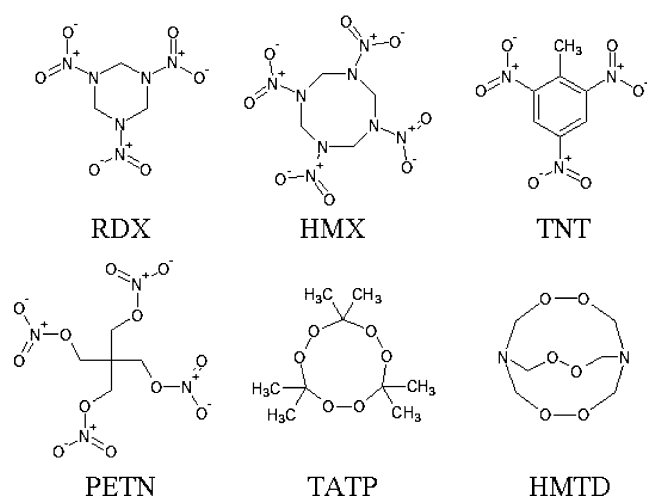

Figure 1. Molecular structure of the six explosives studied: RDX, HMX, TNT, PETN, TATP, and HMTD.

orbitals may play an important role in understanding fluorescence quenching, as adequate orbital overlap of the

acceptor state in the analyte is critical for efficient electron transfer and related fluorescence quenching.[35] The combination of IP, EA, and absorption energies can provide a more complete picture of these molecules fluorescence quenching mechanisms.

Herein, we report the experimentally determined absorptivity of the six molecules and the calculation of the component oscillators from geometry optimized ground states with the application of B3LYP,[36] CAM-B3LYP,[37] ωB97XD,[38] and PBE0.[39] This class of compounds offers a test of current DFT methods, as the systems are highly correlated and involve charge transfer excitations. Each functional was tested against all six explosives with four basis sets to evaluate the effects on both the absorption energy and oscillator strength including: 6-31G(d), 6-31+G(d), 6-31+G(d,p), and 6-311+G(d,p). Utilization of PBE0 for TD-DFT calculations has been shown to be very effective[40] and was found to have the least mean absolute error in a study comparing 500 compounds and 29 functionals.[41] Long range corrected funcitonals like ωB97X and CAM-B3LYP have been reported to improve the prediction of charge transfer excitations.[37] We find good agreement between experimental and TD-DFT determined absorption energies.

2. EXPERIMENTAL AND COMPUTATIONAL METHODS

2.1. Chemical Preparation and Optical Absorption. Solutions (1 mg/mL) of 1,3,5-trinitro-1,3,4-triazinane (RDX), 1,3,5,7-tetranitro-1,3,5,7-tetrazocane (HMX), 2-methyl-1,3,5-trinitrobenzene (TNT), 3-nitrooxy-2,2-bis(nitrooxymethyl)-propyl nitrate (PETN), 3,3,6,6,9,9-hexamethyl-1,2,4,5,7,8-hexoxonane (TATP), and 3,4,8,9,12,13-hexaoxa-1,6-diazabicyclo[4.4.4]tetradecane (HMTD) were made in acetonitrile (CHROMASOLV HPLC gradient grade). Further 1:50 dilutions were prepared for all compounds except TNT, which was diluted 1:100 for UV−vis analysis. UV−vis absorption spectra were collected using a Hewlett-Packard 8452A diode array UV−visible spectrometer with a spectral resolution of 2 nm in a 1 cm quartz cuvette.

2.2. TD-DFT of Singlet Excited States. All calculations were performed using the Gaussian09[42] program on a Sunfire X2200 M2 x64 server (2x Opteron quad core). Calculations were performed on geometry optimized structures in the gas phase. The geometries of the six organic explosive molecules (RDX, β-HMX, TATP, TNT, PETN, and HMTD) were minimized using B3LYP/6-31+G(d,p). The minimized geometries were verified by calculating the vibrational energies to confirm there were no imaginary frequencies. Four TD-DFT methods were compared including: B3LYP, CAM-B3LYP, ωB97XD, and PBE0. For each method, four basis sets were
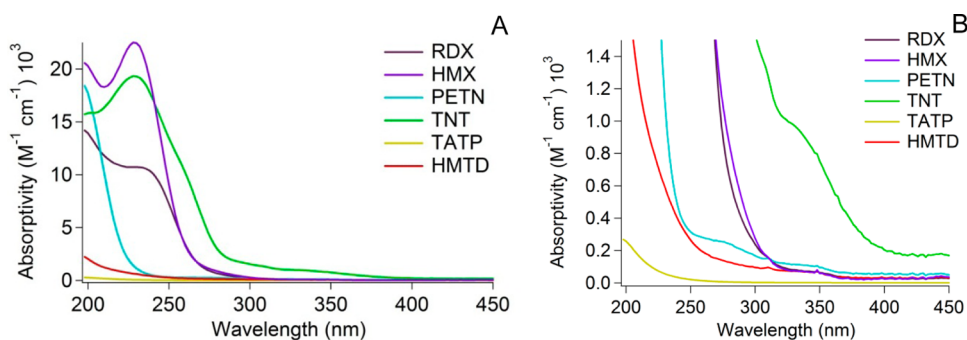

Figure 2. Experimentally determined UV−vis absorption spectra for six explosives: RDX (black), HMX (purple), PETN (cyan), TNT (green), TATP (yellow), and HMTD (red) in the full (A) and expanded (B) perspectives.
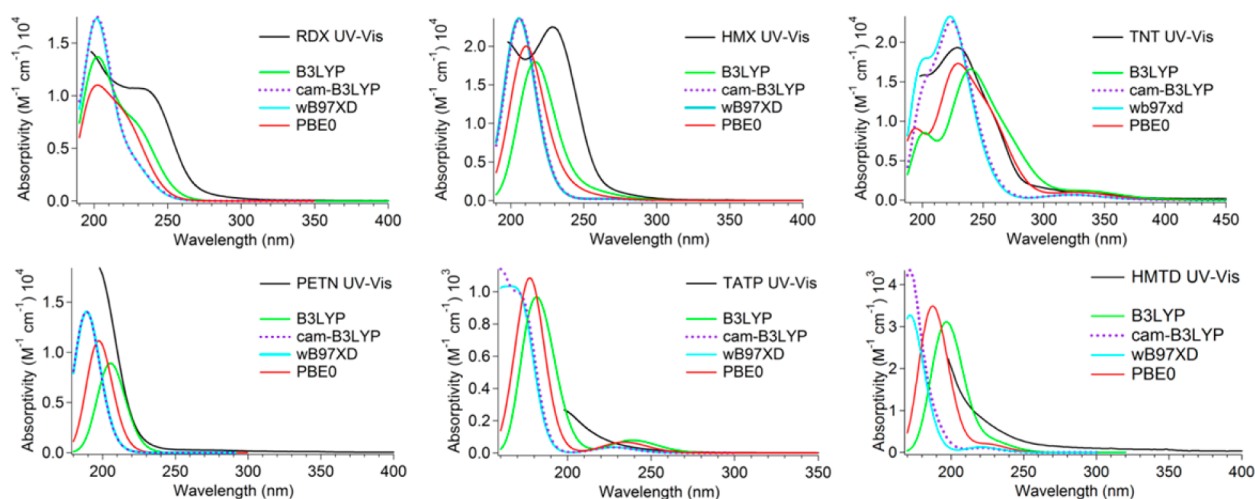
Figure 3. TD-DFT predicted absorption spectra for the six explosives (RDX, HMX, TNT, PETN, TATP, and HMTD) as calculated by B3LYP (green), CAM-B3LYP (dashed-purple), ωB97XD (cyan), and PBE0 (red) using the 6-311+G(d,p) basis set. Spectra were calculated by fitting the predicted oscillators with 0.333 eV HWHM Gaussian peaks and summed to give each trace. Experimentally determined UV−vis spectra were provided in black.

tested for each of the six molecules including: 6-31G(d), 6-31+G(d), 6-31+G(d,p), and 6-311+G(d,p). Vertical absorption energies and oscillator strengths were extracted and fit with a series of Gaussian peaks with a half-width at half-maximum (HWHM) of 0.333 eV, followed by summation of the Gaussian series. This value proved effective at emulating the experimental data. This standard operation was completed using Gauss-View5. Natural transition orbital analysis was conducted using PBE0/6-311+G(d,p).

3. RESULTS AND DISCUSSION

3.1. Optical Absorption. The UV−vis electronic absorption spectra of six explosives were collected in acetonitrile and shown in Figure 2. RDX, HMX, and TNT all exhibited a strong absorption peak near 230 nm. TNT had an additional shoulder around 260 nm and relatively low absorption that extended out to 400 nm. PETN has an absorption maximum at or below 190 nm, whereas TATP and HMTD had an absorption maximum below 190 nm. Each spectrum was fit with a series sum of Gaussian peaks to identify the absorption maximum of separate absorption components. The spectral fits were reported in Figure S1, Supporting Information. The RDX and HMX spectra exhibited similar absorption peaks at 236 and 230 nm with absorptivity of 10 570 and 22 460 M^{-1} cm^{-1}, respectively. The two compounds have negligible absorption at wavelengths longer than 300 nm. PETN exhibited absorption below 235 nm and an absorption max <190 nm, with an absorptivity 10 230 M^{-1} cm^{-1} at 210 nm. The TNT spectrum was more complex than that of the other molecules studied. To model this spectrum, we used a series of five Gaussian peaks with absorption maxima and absorptivity of 198 nm (14 370 M^{-1} cm^{-1}), 229 nm (14 020), 254 nm (10 030), 298 nm (2710), and 326 nm (2670). It is unlikely the 298 nm fit feature is significant, as it could be eliminated through Lorentzian or Voigt fitting. The measured absorptivity at 254 nm was 12 160 M^{-1} cm^{-1}. The low absorption region of the TNT spectrum at wavelength longer than 300 nm can be more easily examined in the expanded absorption spectrum shown in Figure 2(B). TATP had very little recorded absorption (see Figure 2B), with an absorptivity of 260 M^{-1} cm^{-1} at 200 nm. The spectrum

could be fit with two Gaussians with absorption maxima at 194 and 220 nm. HMTD exhibited a very similar absorption spectrum to TATP; however, it had approximately 8 times the absorptivity at 200 nm measured to be 2040 M^{-1} cm^{-1}. The spectrum could also be fit with two Gaussians with absorption maxima at 188 and 226 nm.

3.2. Predicted UV−Vis Spectra. Basis set effects were first evaluated using 6-31G(d), 6-31+G(d), 6-31+G(d,p), and 6-311+G(d,p), in which it was determined a minimal basis set 6-31+G(d) was sufficient to remove significant errors (see Figure S2, Supporting Information, in which PBE0 results of the absorption energies and oscillator strengths as a function of basis set were reported); however, we decided to conduct subsequent calculations with the larger 6-311+G(d,p). For each of the explosives studied, the predicted UV−vis spectra as calculated by TD-DFT methods: B3LYP, CAM-B3LYP, ωB97XD, and PBE0 using the 6-311+G(d,p) basis set were plotted against the experimental UV−vis spectra and reported as Figure 3. The resultant oscillator strength and peak position from the TD-DFT calculations were fit with Gaussian functions and summed to generate the predicted spectra.

B3LYP consistently predicted the lowest transition energies, whereas CAM-B3LYP and ωB97XD were consistently higher than the other methods. The latter two methods produced essentially identical results for all the compounds studied, as can be seen in the RDX, HMX, TATP, and PETN spectra. Slight variations between CAM-B3LYP and ωB97XD in oscillator strength were seen for TNT and HMTD; however, the absorption energies were the same. All the methods failed to predict the 240 nm absorption peak position of RDX and HMX accurately. Instead, this peak appears as a shoulder in the RDX spectra at 225 nm. The oscillator strength of this feature was relatively underpredicted by ωB97XD and CAM-B3LYP but was predicted well by PBE0 and B3LYP. ωB97XD and CAM-B3LYP did not duplicate the 254 nm peak absorption energy that can be seen in the TNT spectrum, whereas PBE0 was in excellent agreement with the experiment.

As PBE0 was in essence an average of the methods tested and performed better in calculating the TNT spectra, we have used this method to study the molecular orbitals involved in selected transitions for the six explosives by NTO analysis.

PBE0 has been previously reported to provide improved results over other DFT functionals.[41] The explosives under study are expected to have solvatochromic behavior which is the likely source of error between experimental and predicted spectra. Future studies may improve results by explicitly including the first solvation shell by MD simulations, as well as including a PCM model in the TD-DFT calculations; see Figure S3, Supporting Information.

3.3. Molecular Orbital Analysis Using Natural Transition Orbitals.

3.3.1. TNT. The experimentally determined absorption spectrum of TNT is presented in Figure 4. As
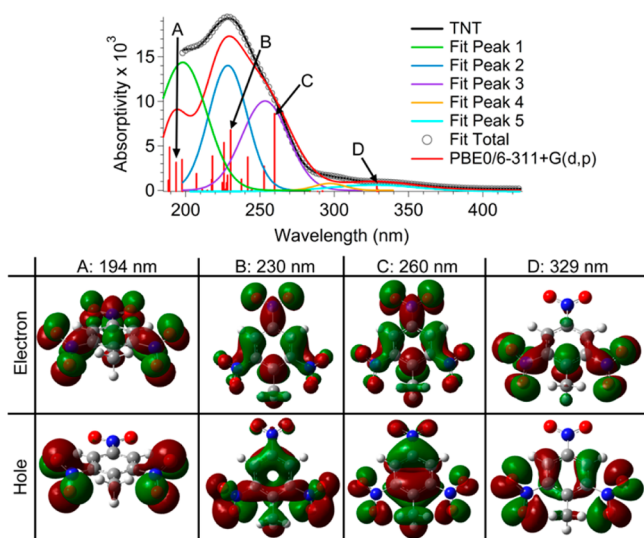

Figure 4. Upper: UV−vis absorption spectra of TNT (black line) as fit by four Gaussian peaks, 1 (green), 2 (blue), 3 (purple), 4 (orange), and 5 (cyan), and the sum of the fit peaks (open gray circles). Also included is the PBE0/6-311+G(d,p) predicted absorption spectra (red), including relative oscillators (vertical lines). (See Figure S2, Supporting Information, for actual values.) Markers A−D point to transitions with the most significant oscillator strength. Lower: natural transition orbitals of the hole and electron orbitals for the transitions corresponding to markers A−D.

previously mentioned, the spectrum was fit with a series of Gaussian functions to deconvolute the component transitions (see Supporting Information Figure S1 for fit). For TNT, five Gaussian line shapes were needed with λ_{max} at 198, 229, 254, 298, and 326 nm. As previously mentioned, it is not clear from this data that the 298 nm peak is a significant feature or if it is an artifact of the data fitting procedure, as the intensity is low
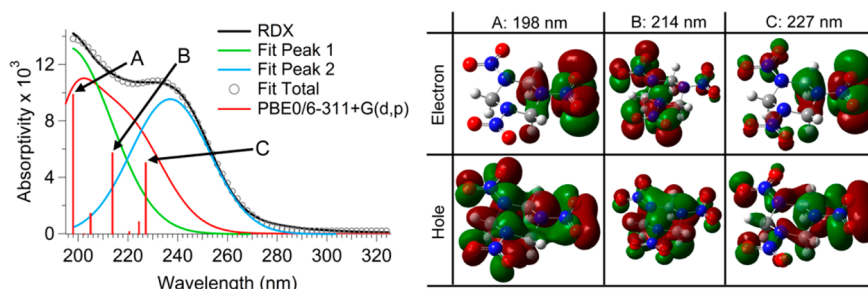
relative to the other Gaussian functions used. The PBE0/6-311+G(d,p) predicted absorption energies and relative oscillator strengths were displayed as vertical red lines. By using a sum of 0.333 eV HWHM Gaussian functions (which is a standard fitting protocol in the GaussView software) for each of the vertical transition energies, the predicted absorption spectrum was generated (solid red line). The resulting spectrum agrees very well with the experimental absorption spectrum. Of the many predicted transitions, four have been selected that are both relatively large in oscillator amplitude and correlate well with the fit peaks. For these four transitions, natural transition orbitals were calculated and plotted in the lower panel of Figure 4.

Transition A (194 nm) has a ground state made up of primarily of O (2p) nonbonding (n) electrons located at the 2,6 positions, whereas the excited state is of O—N=O π^* orbitals at the 2, 6, and 4 position nitro groups forming a charge transfer (CT) excitation. Transition B (230 nm) has a more complicated ground state of ring aromatic π orbitals and O (n) character, whereas the excited state is of π^* states within both the NO_2 and ring groups. Transition C (260 nm) has very similar MO structure both the ground and excited states at the transition B. The $\pi^* \leftarrow \pi$ assignment is consistent with previous reports and solvent dependent absorption energy of this peak.[43] The low oscillator strength transition D (329 nm), which causes the broadening of the absorption spectrum in that region, is of O (n) orbitals at the 2,6 nitro groups in the ground state and NO_2 π^* orbitals of the same 2,6 nitro groups.

3.3.2. RDX. The experimentally determined UV−vis absorption spectrum of RDX (black trace) is presented in Figure 5. The spectrum was fit with two Gaussian functions (green and blue traces) with λ_{max} at 196 and 237 nm. The latter transition has been described to be due to $\pi^* \leftarrow \pi$ transition[44] with the former being attributed to σ, π, σ^*, π^*, and n states.[10] Transition A (198 nm) has a ground state made up of a complicated mixture of states as predicted. It is mostly n in character, with the n states on the oxygens and nitrogens, which mix to form an extended pseudo-π system across the whole molecule. The excited state is simply the N−NO_2 π^* states, the transition of which as a result is clearly CT in nature. Likewise, transition B (214 nm) is an interesting π system created by the ring N atoms mixed with C−H and C−C σ bonds and some occupation due to O n states. Once again, the excited state is due to the N−NO_2 π^* orbitals; however, it is more equally distributed across the molecule than transition A. Finally, transition C (227 nm) is made up of mostly O n states mixed with the ring N n states; however, there is also some N−N and
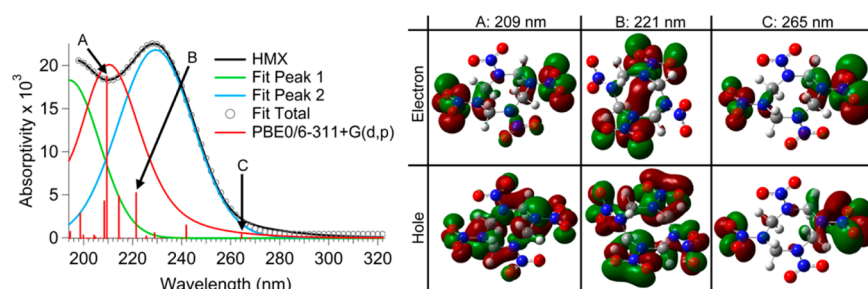

Figure 5. Left: UV−vis absorption spectra of RDX (black line) as fit by two Gaussian peaks, 1 (green) and 2 (blue), and the sum of the fit peaks (open gray circles). Also included is the PBE0/6-311+G(d,p) predicted absorption spectra (red), including relative oscillators (vertical lines). (See Figure S2, Supporting Information, for actual values.) Markers A−C point to transitions with the most significant oscillator strength. Right: natural transition orbitals of the hole and electron orbitals for the transitions corresponding to markers A−C.

Figure 6. Left: UV−vis absorption spectra of HMX (black line) as fit by two Gaussian peaks, 1 (green), and 2 (blue), and the sum of the fit peaks (open gray circles). Also included is the PBE0/6-311+G(d,p) predicted absorption spectra (red), including relative oscillators (vertical lines). (See Figure S2, Supporting Information, for actual values.) Markers A−C point to transitions with the most significant or relevant oscillator strength. Right: natural transition orbitals of the hole and electron orbitals for the transitions corresponding to markers A−C.
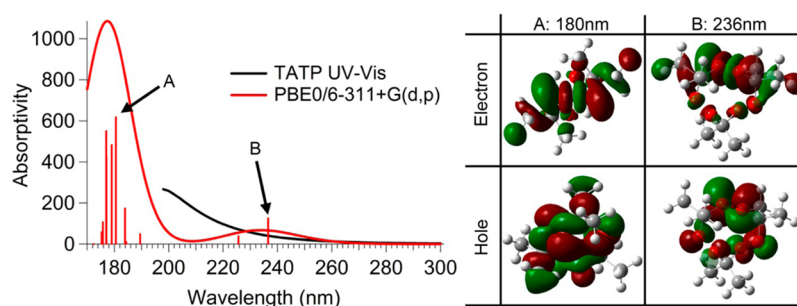

Figure 7. Left: UV−vis absorption spectra of TATP (black line) as well as the PBE0/6-311+G(d,p) predicted absorption spectra (red), including relative oscillators (vertical lines). (See Figure S2, Supporting Information, for actual values.) Marker A points to the transition with the most significant oscillator strength and marker B points to a lower energy transition. Right: natural transition orbitals of the hole and electron orbitals for the transitions corresponding to marker A and B.
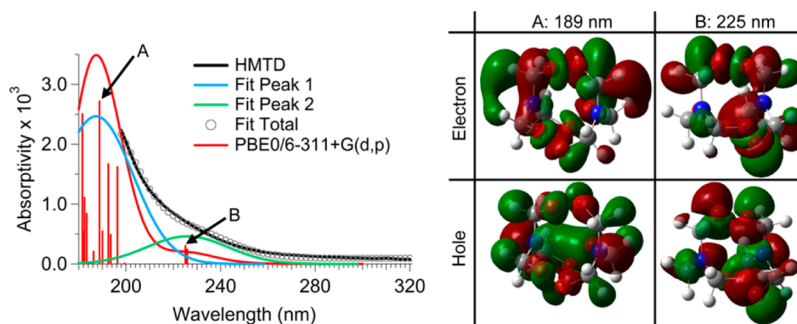

Figure 8. Left: UV−vis absorption spectra of HMTD (black line) as fit by two Gaussian peaks, 1 (blue) and 2 (green), and the sum of the fit peaks (open gray circles). Also included is the PBE0/6-311+G(d,p) predicted absorption spectra (red), including relative oscillators (vertical lines). (See Figure S2, Supporting Information, for actual values.) Markers A and B point to transitions of interest. Right: natural transition orbitals of the hole and electron orbitals for the transitions corresponding to markers A and B.

C−H σ bond character as well. The excited state is again the N−NO$_2$ π^* orbitals.

3.3.3. HMX. The UV−vis spectrum for HMX is presented in Figure 6 (black trace) along with a two Gaussian functions fit using λ_{max} at 194 and 229 nm. The PBE0/6-311+G(d,p) predicted absorption energies and relative oscillator strengths are reported (red vertical lines) as well as the reconstructed absorption spectrum (red trace). Three absorption energies of interest were selected (A−C). The molecular orbitals relating to each transition are shown in Figure 6 as well.

Transition A (209 nm) has a complicated ground state electronic structure consisting of O and N nonbonding with a small portion of C−H σ bonding electrons. The excited state is from N−NO$_2$ π^* orbitals of the nitro groups which were planar to the ring structure. Much of the electron density in the A

ground state is ring centered, whereas the electron density of the excited state is localized on the NO$_2$ groups as a CT type excitation. The ground state of transition B (221 nm) was made up of O and ring N n states, whereas the excited state was again made up of the N−NO$_2$ π^* orbitals of the perpendicular nitro groups this time. Interestingly, there was a σ bond formed between the two ring N atoms made by the p orbitals, which with respect to the N−NO$_2$ group were antibonding but to each other formed a bonding interaction. Finally, transition C, which was low in oscillator strength in comparison to the others discussed, had a ground state made of the planar nitro group n states of O, whereas the excited state was again the planar N−NO$_2$ π^* states.

3.3.4. TATP. Figure 7 shows electronic absorption of TATP (black track). The molecule had negligible absorptivity

compared to the other molecules studied. The experimentally determined spectrum was not fit as the result would be meaningless. The predicted absorption energy and relative oscillator strength as calculated by PBE0/6311+G(d,p) was presented, as well as the reconstructed absorption spectrum (red). MO analysis of the transition labeled A shows a ground state of a mixed π and π^* character derived from the nonbonding oxygen orbitals, whereas the excited state is a O$-$O σ^* bond. The oscillator labeled B was due to a transition between O nonbonding states and an O$-$O σ^* bond.

3.3.5. HMTD. Electronic absorption of HMTD (black trace) is shown in Figure 8 and fit with two Gaussian functions centered at 188 and 226 nm (blue and green traces). Although this fit is certainly not unique, it did match nicely to the predicted spectrum and was left in for Figure 8 as a visual aid. The PBE0/6-311+G(d,p) predicted absorption energies and relative oscillator strengths, as well as the reconstructed absorption spectrum, is presented (red) in which two transitions, A and B, have thusly been labeled. The molecular orbitals for these two labeled transitions are also presented.

The ground state of transition A (189 nm) has an interesting structure made of a relatively small contribution from C$-$O σ bonds, but a majority contribution from two N atoms n orbitals that point into the center of the molecule. The excited state was the O$-$O σ^* orbital, with a small component due to a localized antibonding σ^* configuration between the two N atoms. Transition B shows contributions from both N and O nonbonding orbitals to the O$-$O σ^* states in the excited state.

3.3.6. PETN. The experimental UV$-$vis spectrum of PETN (black trace) is shown in Figure 9 along with a single Gaussian
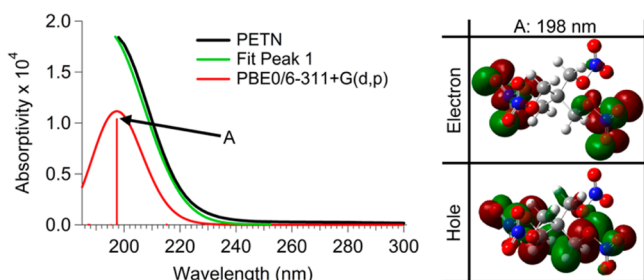

Figure 9. Left: UV$-$vis absorption spectra of PETN (black line) as fit by one Gaussian peak (green). Also included is the PBE0/6-311+G(d,p) predicted absorption spectra (red), including relative oscillators (vertical lines). (See Figure S2, Supporting Information, for actual values.) Marker A points to the only transition. Right: natural transition orbitals of the hole and electron orbitals for the transitions corresponding to A.

fit centered at 194 nm. The absorption in this region has been assigned to a $\pi^* \leftarrow \pi$ transition with CT from the carbon backbone to the NO$_2$ groups.[45] The PBE0 6-311+G(d,p) absorption energies and reconstructed absorption spectrum is presented in Figure 9 as well. It should be noted that previous reports[45] have found a shoulder in the absorption spectrum at 260$-$290 nm due to a $\pi^* \leftarrow n$ transition of the $-$NO$_2$ groups; however, none of the TD-DFT methods tested calculated a nonzero oscillator in this region (though a zero oscillator was calculated for a 256 nm transition, which did correspond to an $\pi^* \leftarrow n$ transition). A shoulder appearing at $\sim$260 nm was observed in our absorption spectrum at very low relative intensity (see Figure 2 expanded view). The transition labeled A (198 nm) also corresponded to a ground state of C$-$H σ

bonding and O nonbonding states, whereas the excited state was O$-$NO$_2$ π^* antibonding orbitals in which charge was transferred from the carbon backbone to the distal NO$_2$ groups.

3.4. Energy Levels. By combining the vertical ionization potentials (IP$_V$) calculated by CBS-QB3 with Koopmans' theorem in our previous work[33] and the absorption energies calculated herein, we have constructed an energy level diagram for each of the six explosive molecules, as shown in Figure 10.
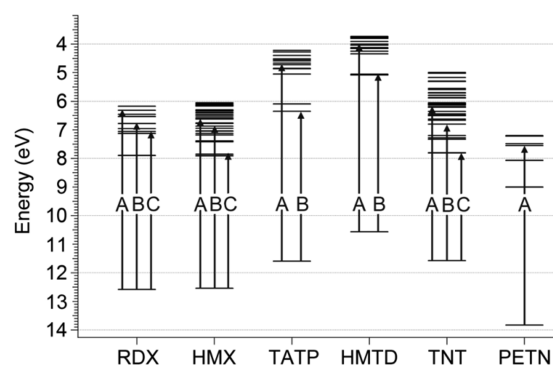

Figure 10. Calculated energy level diagrams for the six explosives: RDX, HMX, TATP, HMTD, TNT, and PETN. Ground state energy (HOMO) is considered equal to the vertical ionization potential (IP$_V$) taken from Cooper et al.[33] as calculated by CBS-QB3. Excited states were calculated herein by TD-DFT with PBE0/6-311+G(d,p). Letters labeling transitions are the same labels used in Figures 4$-$9 to highlight significant contributions to the absorption spectrum.

For ease of comparison, the transitions described in Figures 4$-$9 have been indicated in Figure 10. For RDX, TATP, HMTD, and PETN, the lowest 15 singlet transition energies are shown, whereas for HMX and TNT, the first 40 are indicated. The lowest energy shown is the highest occupied molecular orbital (HOMO) and the first vertical transitions with significant oscillator strength (see Figure S2, Supporting Information) for HMX, TATP, HMTD, and TNT is the lowest unoccupied molecular orbital (LUMO). For RDX and PETN, the LUMO transition is dark, having zero oscillator strength.

These results should be useful in the design and optimization of explosives detection methods utilizing fluorescence quenching, as the unoccupied energy levels can act as acceptor states from the fluorescent probe. For II$-$VI QD probes, the CB energies for CdTe, CdSe, CdS, ZnTe, ZnSe, and ZnS are all <5 eV vs vacuum,[46,47] making them all likely candidates for fluorescence quenching by the explosive analytes, as all the explosives have a manifold of acceptor states in this range; however, possible issues in designing such systems are worth mentioning.
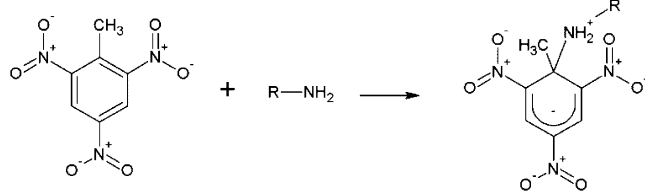
One potential issue could be that RDX, HMX, TNT, and PETN all have exothermic electron affinities between 0.1 and 0.75 eV, whereas TATP and HMTD have identical endothermic affinities of $-$1.12 eV. Additionally, RDX, HMX, TATP, and HMTD were seen to have unstable geometries in their reduced forms.[33] Therefore, the charge transfer step from QD $\rightarrow$ explosive could cause degradation of RDX and HMX analyte consequently resulting in a different fluorescence quenching mechanism than has been previously discussed insofar that the energy level alignment for electron transfer and back transfer between QD and explosive may not be applicable and thus warrants further investigation.

A second issue could be band alignment with the VB of the QD, as an injected electron from the QD to an acceptor state in

the explosive could decay to the LUMO level rapidly before back-transfer can take place. To minimize potentially destructive reduction of the analyte by the QD and to optimize the QD quenching stability over time, the back electron transfer should be favorable. This would place a restriction on materials with VB levels below the LUMO level of the explosive analyte. PETN has a LUMO level of 9.00 eV excluding any II−VI semiconductor. RDX, HMX, and TNT (see section 3.5 about TNT-Meisenheimer complexes) have similar LUMO levels at about 8 eV, which leaves ZnO as the only candidate of II−VI semiconductors. For TATP, the LUMO was calculated to be 6.35 eV; II−VI materials with VB edges lower than the LUMO are ZnS, ZnSe, CdS, and CdSe. HMTD has more flexibility in materials choices having a LUMO level of 5.08 eV, which includes the above listed materials plus ZnTe and CdTe. Assuming fluorescence quenching is possible with TATP and HMTD and that the CB energy is relevant to the mechanism, one could design a fluorescence assay to distinguish between an unknown sample of peroxide based explosive.

3.5. Meisenheimer Complex. As previously stated, QD based methods targeting TNT have utilized surface bound primary amines, which when exposed to TNT form a Meisenheimer complex, Scheme 1.[17,18,22] From our predictions,

Scheme 1. Formation of a Meisenheimer Complex from the Reaction of 2,4,6-Trinitrotoluene with a Primary Amine

it does not appear that TNT is capable of quenching materials like CdSe, CdS, ZnSe, or ZnS. Therefore, the formation of this complex could be more significant to the quenching mechanism than previously thought. The rational design of using QD surface bound primary amines has been proposed as a binding mechanism of the TNT to the QD surface so efficient quenching can take place; consequently, it is likely the resulting energy levels of the TNT change dramatically to allow for electron transfer to occur.

To confirm this point, we have investigated the Meisenheimer complex formed between 2,4,6-trinitrotoluene and propylamine (TNT-M). Optimization of the structure was performed with B3LYP/6-31+G(d,p) and a vibrational spectrum was calculated to confirm that the minimized structure was reached. The reaction enthalpy of Scheme 1 where R = $(CH_2CH_2CH_3)$ as calculated with B2PLYPD/6-311+G(3df,2p) was −20.22 kJ mol⁻¹. Assuming the contribution from entropy to be small, the equilibrium constant (K_{eq}) for this reaction would be 3.5×10^3 in vacuum. This value is in good agreement with Sharma et al.[48] in which the TNT + isopropylamine complex K_{eq} was reported to be 2.94×10^4 in DMSO.

The ionization energy (IE) was calculated using Koopmans' theory[33] by MP2/6-311+G(3df,2p) and found to be 8.727 eV and the exothermic electron affinity (EA) was 0.093 eV. The IE energy of the complex represents a 2.74 eV shift compared to TNT whereas the EA of the two were within 0.1 eV of each other. TD-DFT calculations were performed using PBE0/6-

311+G(d,p) in which the absorption energies and oscillator strength, given in parentheses, for the first 4 singlet excitations were found to be 2.64 eV (0.1987), 3.46 eV (0.2069), 3.62 eV (0.0004), and 3.76 eV (0.0001). The predicted UV−vis spectra of TNT and TNT-M were reported in Figure 11. These results
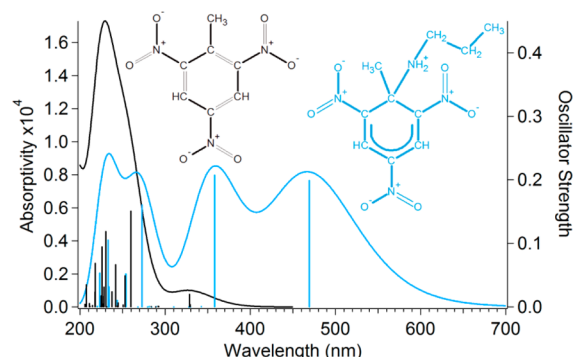
Figure 11. Predicted UV−vis spectrum of TNT (black) and a TNT Meisenheimer complex with propylamine (blue) with TD-DFT PBE0/6-311+G(d,p). Solid traces correspond to units of absorptivity (left axis), and vertical lines relate to the oscillator strength (right axis).

place the HOMO and LUMO level at 8.727 and 6.09 eV, respectively. With this shift in the LUMO energy level, quenching of QD systems is much more likely. This observation apparently confirms our conclusions regarding semiconductor selections and the role of the Meisenheimer complex in the quenching reaction.

Additional observations of QD fluorescent quenching by 2,4,6-trinitrophenol (picric acid) have been reported. The Meisenheimer complex formed between picric acid (PA) and propylamine was examined in which the reaction enthalpy was calculated with B2PLYPD/6-311+G(3df,2p) and was −8.86 kJ mol⁻¹. This is 11.36 kJ mol⁻¹ less than the Meisenheimer complex formed with TNT. Therefore, the expected ratio of Meisenheimer formation of TNT to PA is ∼10:1. The IE and EA of PA were calculated by MP2/6-311+G(3df,2p) which were 11.214 and 0.583 eV as well as the picric acid Meisenheimer complex (PA-M), which were 9.121 and 0.194 eV, respectively. The first four singlet excitation absorption energies and (oscillator strengths) were calculated with TD-DFT PBE0/6-311+G(d,p) and were 2.82 eV (0.203), 3.61 (0.186), 3.74 (0.003), and 3.824 (0.000). The predicted UV−vis spectra of both the PA and PA-M complex were reported in Figure 12. The LUMO level shift of the PA is very similar to that of the TNT-M complex. These results indicate that PA will quench QD PL less effectively than TNT, which is consistent with some[18,20,25] and contradictory to other[21] reports. The energy level diagram of the TNT, TNT-M, PA, and PA-M was presented in Figure 13.

4. CONCLUSIONS

We have calculated the singlet excitations of six common explosives, RDX, β-HMX, TATP, HMTD, TNT, and PETN, by TD-DFT methods including PBE0, ωB97XD, CAM-B3LYP, and B3LYP with several basis sets including 6-31G(d), 6-31+G(d), 6-31+G(d,p), and 6-311+G(d,p). The best agreement between experimentally determined absorption energies and those calculated by TD-DFT was with the PBE0 functional, with the smallest basis set of 6-31+G(d); however, all analysis was performed at the higher 6-311+G(d,p). In general, the
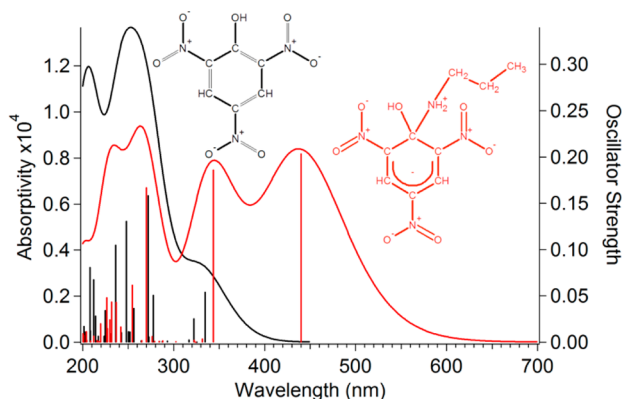
Figure 12. Predicted UV−vis spectrum of picric acid (black) and a picric acid Meisenheimer complex formed with propylamine (red) with TD-DFT PBE0/6-311+G(d,p). Solid traces correspond to units of absorptivity (left axis), and vertical lines relate to the oscillator strength (right axis).
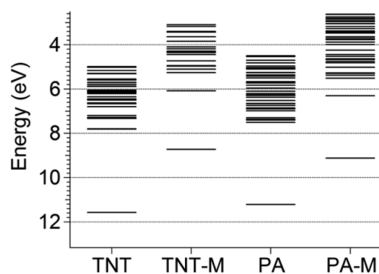

Figure 13. Energy level diagram of TNT, TNT Meisenheimer complex formed between TNT and propylamine (TNT-M), picric acid (PA), and picric acid Meisenheimer complex with propylamine (PA-M). The lowest energy level, corresponding to the HOMO, was calculated by MP2/6-311+G(3df,2p) and determined using Koopmans' theory. Unoccupied energy levels were determined by TD-DFT PBE0/6-311+G(d,p).

long-range corrected ωB97XD and CAM-B3LYP functionals performed identically in most cases and tended to predict higher absorption energies than PBE0 or B3LYP, whereas B3LYP predicted the lowest energy excitations. Natural transition orbitals were calculated for the major contributing oscillator components to the absorption spectra with PBE0/6-311+G(d,p). The results offer visualization of the hole and electron densities associated with UV to deep UV absorption. By combining IP_V at the CBS-QB3 level and TD-DFT, energy level diagrams were reported for each of the six compounds. The energy level diagram can be utilized to assist in designing fluorescence quenching detection methods that utilize a donor/acceptor model like those proposed in QD and fluorescent polymer probe studies. Analysis of TNT and picric acid (PA) Meisenheimer complexes indicate the energetic shift of the HOMO level is responsible for the QD PL quenching observed whereas the uncoordinated TNT and PA are not predicted to be efficient quenchers for any II−VI semiconductor system except ZnO.

■ ASSOCIATED CONTENT

Ⓢ Supporting Information

Figures of fits for experimental UV−vis spectra, of absorption energies, and of calculated UV−vis spectra. This information is available free of charge via the Internet at http://pubs.acs.org

■ AUTHOR INFORMATION

Corresponding Author
*C.D.G.: phone, 925-424-5951; e-mail, grant29@llnl.gov. J.Z.Z.: phone, 831-459-3776; e-mail, zhang@ucsc.edu.

Notes
The authors declare no competing financial interest.

■ REFERENCES

(1) Mullen, C.; Huestis, D.; Coggiola, M.; Oser, H. Laser Photoionization of Triacetone Triperoxide (TATP) by Femtosecond and Nanosecond Laser Pulses. *Int. J. Mass Spectrom.* **2006**, *252*, 69−72.

(2) Mullen, C.; Irwin, A.; Pond, B. V.; Huestis, D. L.; Coggiola, M. J.; Oser, H. Detection of Explosives and Explosives-Related Compounds by Single Photon Laser Ionization Time-of-Flight Mass Spectrometry. *Anal. Chem.* **2006**, *78*, 3807−3814.

(3) Marshall, A.; Clark, A.; Jennings, R.; Ledingham, K. W. D.; Sander, J.; Singhal, R. P. Laser-Induced Dissociation, Ionization and Fragmentation Processes in Nitroaromatic Molecules. *Int. J. Mass Spectrom. Ion Processes* **1992**, *116*, 143−156.

(4) Cabalo, J.; Sausa, R. Trace Detection of Explosives with Low Vapor Emissions by Laser Surface Photofragmentation-Fragment Detection Spectroscopy with an Improved Ionization Probe. *Appl. Opt.* **2005**, *44*, 1084−1091.

(5) Oxley, J. C.; Smith, J. L.; Kirschenbaum, L. J.; Marimganti, S.; Vadlamannati, S. Detection of Explosives in Hair Using Ion Mobility Spectrometry. *J. Forensic Sci.* **2008**, *53*, 690−693.

(6) Creaser, C. S.; Griffiths, J. R.; Bramwell, C. J.; Noreen, S.; Hill, C. A.; Thomas, C. L. P. Ion Mobility Spectrometry: A Review. Part 1. Structural Analysis by Mobility Measurement. *Analyst* **2004**, *129*, 984−994.

(7) Borch, T.; Gerlach, R. Use of Reversed-Phase High-Performance Liquid Chromatography−diode Array Detection for Complete Separation of 2, 4, 6-Trinitrotoluene Metabolites and EPA Method 8330 Explosives: Influence of Temperature and an Ion-Pair Reagent. *J. Chromatogr., A* **2004**, *1022*, 83−94.

(8) Schulte-Ladbeck, R.; Kolla, P.; Karst, U. Trace Analysis of Peroxide-Based Explosives. *Anal. Chem.* **2003**, *75*, 731−735.

(9) Crowson, A.; Beardah, M. S. Development of an LC/MS Method for the Trace Analysis of Hexamethylenetriperoxidediamine (HMTD). *Analyst* **2001**, *126*, 1689−1693.

(10) Tuschel, D. D.; Mikhonin, A. V.; Lemoff, B. E.; Asher, S. A. Deep Ultraviolet Resonance Raman Excitation Enables Explosives Detection. *Appl. Spectrosc.* **2010**, *64*, 425−432.

(11) Fang, X.; Ahmad, S. Detection of Explosive Vapour Using Surface-Enhanced Raman Spectroscopy. *Appl. Phys. B: Lasers Opt.* **2009**, *97*, 723−726.

(12) Lin, H.; Suslick, K. S. A Colorimetric Sensor Array for Detection of Triacetone Triperoxide Vapor. *J. Am. Chem. Soc.* **2010**, *132*, 15519−15521.

(13) Reynolds, J.; Nunes, P.; Whipple, R.; Alcaraz, A. In *Detection and Disposal of Improvised Explosives*; Schubert, H., Kuznetsov, A., Eds.; Springer: The Netherlands, 2006; Vol. 6, pp 27−32.

(14) Germain, M. E.; Knapp, M. J. Turn-on Fluorescence Detection of H2O2 and TATP. *Inorg. Chem.* **2008**, *47*, 9748−9750.

(15) Gao, D.; Wang, Z.; Liu, B.; Ni, L.; Wu, M.; Zhang, Z. Resonance Energy Transfer-Amplifying Fluorescence Quenching at the Surface of

Silica Nanoparticles toward Ultrasensitive Detection of TNT. *Anal. Chem.* **2008**, *80*, 8545−8553.

(16) Shi, G. H.; Shang, Z. B.; Wang, Y.; Jin, W. J.; Zhang, T. C. Fluorescence Quenching of CdSe Quantum Dots by Nitroaromatic Explosives and Their Relative Compounds. *Spectrochim. Acta Part A* **2008**, *70*, 247−252.

(17) Zhang, K.; Zhou, H.; Mei, Q.; Wang, S.; Guan, G.; Liu, R.; Zhang, J.; Zhang, Z. Instant Visual Detection of Trinitrotoluene Particulates on Various Surfaces by Ratiometric Fluorescence of Dual-Emission Quantum Dots Hybrid. *J. Am. Chem. Soc.* **2011**.

(18) Chen, Y.; Chen, Z.; He, Y.; Lin, H.; Sheng, P.; Liu, C.; Luo, S.; Cai, Q. L-Cysteine-Capped CdTe QS-Based Sensor for Simple and Selective Detection of Trinitrotoluene. *Nanotechnology* **2010**, *21*, 125502.

(19) Xia, Y.; Song, L.; Zhu, C. Turn-On and Near-Infrared Fluorescent Sensing for 2, 4, 6-Trinitrotoluene Based on Hybrid (Gold Nanorod)-(Quantum Dots) Assembly. *Anal. Chem.* **2011**, *83*, 1401−1407.

(20) Freeman, R.; Finder, T.; Bahshi, L.; Gill, R.; Willner, I. Functionalized CdSe/ZnS QDs for the Detection of Nitroaromatic or RDX Explosives. *Adv. Mater. (Weinheim, Ger.)* **2012**, *24*, 6416−6421.

(21) Tu, R.; Liu, B.; Wang, Z.; Gao, D.; Wang, F.; Fang, Q.; Zhang, Z. Amine-Capped ZnS-Mn2+ Nanocrystals for Fluorescence Detection of Trace TNT Explosive. *Anal. Chem.* **2008**, *80*, 3458−3465.

(22) Fant, F.; De Sloovere, A.; Matthijsen, K.; Marlé, C.; El Fantroussi, S.; Verstraete, W. The Use of Amino Compounds for Binding 2,4,6-Trinitrotoluene in Water. *Environ. Pollut.* **2001**, *111*, 503−507.

(23) McQuade, D. T.; Pullen, A. E.; Swager, T. M. Conjugated Polymer-Based Chemical Sensors. *Chem. Rev.* **2000**, *100*, 2537−2574.

(24) Sohn, H.; Calhoun, R. M.; Sailor, M. J.; Trogler, W. C. Detection of TNT and Picric Acid on Surfaces and in Seawater by Using Photoluminescent Polysiloles. *Angew. Chem., Int. Ed.* **2001**, *40*, 2104−2105.

(25) Sanchez, J. C.; Trogler, W. C. Efficient Blue-Emitting Silafluorene−fluorene-Conjugated Copolymers: Selective Turn-off/ Turn-on Detection of Explosives. *J. Mater. Chem.* **2008**, *18*, 3143−3156.

(26) Sanchez, J. C.; DiPasquale, A. G.; Rheingold, A. L.; Trogler, W. C. Synthesis, Luminescence Properties, and Explosives Sensing with 1, 1-Tetraphenylsilole-and 1, 1-Silafluorene-vinylene Polymers. *Chem. Mater.* **2007**, *19*, 6459−6470.

(27) Toal, S. J.; Magde, D.; Trogler, W. C. Luminescent Oligo (Tetraphenyl) Silole Nanoparticles As Chemical Sensors for Aqueous TNT. *Chem. Commun.* **2005**, *1*, 5465−5467.

(28) Sohn, H.; Sailor, M. J.; Magde, D.; Trogler, W. C. Detection of Nitroaromatic Explosives Based on Photoluminescent Polymers Containing Metalloles. *J. Am. Chem. Soc.* **2003**, *125*, 3821−3830.

(29) Martinez, H. P.; Grant, C. D.; Reynolds, J. G.; Trogler, W. C. Silica Anchored Fluorescent Organosilicon Polymers for Explosives Separation and Detection. *J. Mater. Chem.* **2012**, *22*, 2908−2914.

(30) Weickhardt, C.; Tönnies, K. Short Pulse Laser Mass Spectrometry of Nitrotoluenes: Ionization and Fragmentation Behavior. *Rapid Commun. Mass Spectrom.* **2002**, *16*, 442−446.

(31) Hankin, S. M.; Tasker, A. D.; Robson, L.; Ledingham, K. W. D.; Fang, X.; McKenna, P.; McCanny, T.; Singhal, R. P.; Kosmidis, C.; Tzallas, P.; et al. Femtosecond Laser Time-of-Flight Mass Spectrometry of Labile Molecular Analytes: Laser-Desorbed Nitro-Aromatic Molecules. *Rapid Commun. Mass Spectrom.* **2002**, *16*, 111−116.

(32) Strehmel, B.; Sarker, A. M.; Detert, H. The Influence of σ and π Acceptors on Two-Photon Absorption and Solvatochromism of Dipolar and Quadrupolar Unsaturated Organic Compounds. *ChemPhysChem* **2003**, *4*, 249−259.

(33) Cooper, J. K.; Grant, C. D.; Zhang, J. Z. Ab Initio Calculation of Ionization Potential and Electron Affinity of Six Common Explosive Compounds. *Rep. Theor. Chem.* **2012**, *1*, 11−19.

(34) Martin, R. L. Natural Transition Orbitals. *J. Chem. Phys.* **2003**, *118*, 4775.

(35) Jakubikova, E.; Snoeberger Iii, R. C.; Batista, V. S.; Martin, R. L.; Batista, E. R. Interfacial Electron Transfer in TiO2 Surfaces Sensitized with Ru(II)−Polypyridine Complexes. *J. Phys. Chem. A* **2009**, *113*, 12532−12540.

(36) Becke, A. D. Density-Functional Thermochemistry. IV. A New Dynamical Correlation Functional and Implications for Exact-Exchange Mixing. *J. Chem. Phys.* **1996**, *104*, 1040.

(37) Yanai, T.; Tew, D. P.; Handy, N. C. A New Hybrid Exchange−correlation Functional Using the Coulomb-Attenuating Method (CAM-B3LYP). *Chem. Phys. Lett.* **2004**, *393*, 51−57.

(38) Chai, J. D.; Head-Gordon, M. Long-Range Corrected Hybrid Density Functionals with Damped Atom−atom Dispersion Corrections. *Phys. Chem. Chem. Phys.* **2008**, *10*, 6615−6620.

(39) Adamo, C.; Barone, V. Toward Reliable Density Functional Methods without Adjustable Parameters: The PBE0 Model. *J. Chem. Phys.* **1999**, *110*, 6158.

(40) Adamo, C.; Scuseria, G. E.; Barone, V. Accurate Excitation Energies from Time-Dependent Density Functional Theory: Assessing the PBE0 Model. *J. Chem. Phys.* **1999**, *111*, 2889.

(41) Jacquemin, D.; Wathelet, V.; Perpète, E. A.; Adamo, C. Extensive TD-DFT Benchmark: Singlet-Excited States of Organic Molecules. *J. Chem. Theory Comput.* **2009**, *5*, 2420−2435.

(42) Frisch, M. J.; Trucks, G. W.; Schlegel, H. B.; Scuseria, G. E.; Robb, M. A.; Cheeseman, J. R.; Scalmani, G.; Barone, V.; Mennucci, B.; Petersson, G. A.; et al. *Gaussian 09*; Gaussian: Wallingford, CT, 2009.

(43) Sandus, O.; Slagg, N. Mechanism of the Formation of Pink Water. *DTIC Document*, 1978.

(44) Stals, J.; Barraclough, C. G.; Buchanan, A. S. Molecular orbital interpretation of the ultra-violet absorption spectra of unconjugated aliphatic nitramines. *Trans. Faraday Soc.* **1969**, *65*, 904−914.

(45) Mullen, P. A.; Orloff, M. K. Ultraviolet Absorption Spectrum of Pentaerythritol Tetranitrate. *J. Phys. Chem.* **1973**, *77*, 910−911.

(46) Walukiewicz, W. Intrinsic Limitations to the Doping of Wide-Gap Semiconductors. *Phys. B (Amsterdam, Neth.)* **2001**, *302−303*, 123−134.

(47) Van de Walle, C. G.; Neugebauer, J. Universal Alignment of Hydrogen Levels in Semiconductors, Insulators and Solutions. *Nature* **2003**, *423*, 626−628.

(48) Sharma, S.; Lahiri, S. Absorption Spectroscopic and FTIR Studies on EDA Complexes between TNT (2, 4, 6-Trinitrotoluene) with Amines in DMSO and Determination of the Vertical Electron Affinity of TNT. *Spectrochim. Acta Part A* **2008**, *70*, 144−153.